OPEN

Collective Structural Changes in Vermiculite Clay Suspensions Induced by Cesium Ions

Ryuhei Motokawa[1], Hitoshi Endo[2,3], Shingo Yokoyama[4], Shotaro Nishitsuji[5], Tohru Kobayashi[1], Shinichi Suzuki[1] & Tsuyoshi Yaita[1]

[1]Actinide Coordination Chemistry Group, Quantum Beam Science Center (QuBS), Japan Atomic Energy Agency (JAEA), Tokai, Ibaraki 319-1195, Japan, [2]Neutron Science Division, Institute of Material Structure Science, High Energy Accelerator Research Organization, 203-1 Shirakata, Tokai, Ibaraki 319-1106, Japan, [3]Department of Material Structure Science, The Graduate University for Advanced Studies (SOKENDAI), 203-1 Shirakata, Tokai, Ibaraki 319-1106, Japan, [4]Central Research Institute of the Electric Power Industry, Abiko, Chiba 270-1194, Japan, [5]Graduate School of Science and Engineering, Yamagata University, Yonezawa, Yamagata 992-8510, Japan.

Following the Fukushima Daiichi nuclear disaster in 2011, Cs radioisotopes have been dispersed over a wide area. Most of the Cs has remained on the surface of the soil because Cs^+ is strongly adsorbed in the interlayer spaces of soil clays, particularly vermiculite. We have investigated the microscopic structure of an aqueous suspension of vermiculite clay over a wide length scale (1–1000 Å) by small-angle X-ray scattering. We determined the effect of the adsorption behavior of Cs^+ on the structural changes in the clay. It was found that the abruption of the clay sheets was induced by the localization of Cs^+ at the interlayer. This work provides important information for predicting the environmental fate of radioactive Cs in polluted areas, and for developing methods to extract Cs from the soil and reduce radioactivity.

Following the Fukushima Daiichi nuclear disaster in 2011, a considerable amount of research has focused on removing radioactive cesium isotopes (^{134}Cs and ^{137}Cs) from soil and reducing radioactivity in contaminated areas[1–11]. Cs^+ interacts strongly and selectively with phyllosilicate soil fractions, such as vermiculite and smectite[12–18], which consist of a layered structure of 2 : 1 phyllosilicate clay. Cs^+ rigidly packs into the center of the six-membered rings in the upper and lower SiO_4 tetrahedral sheets across the interlayers, where the characteristic configuration is attributed to the high affinity between the Cs^+ and the clay. In particular, Cs^+ desorption from vermiculite is difficult because Cs^+ binds to the clay interlayer spaces semipermanently[19,20]. The frayed-edge planar site conceptual model is often used to explain the high affinity of Cs^+ for clay[11,20–25], although there is no direct experimental evidence for the structure. The relationship between Cs^+ adsorption to the clay and the clay microscopic structure remains unexplained in many respects and has yet to be studied more closely based on empirical data.

Ionic exchange of Cs^+ with the hydrated or dehydrated alkali metal and alkaline earth metal cations[26,27] that originally occupy the clay interlayer space probably occurs in suspensions. Therefore, investigating the microscopic structure of vermiculite in suspension and the structural changes induced by Cs^+ adsorption should provide important information for treating contaminated soil. In contrast to electron microscopy techniques, X-ray scattering can be used to observe clay suspensions without pre-treatments that require drying. Moreover, the scale of the small-angle X-ray scattering (SAXS) measurements in this study was between 1 and 1000 Å, which corresponds well to the scale of the layer structure and its spatial arrangement in the clay crystal domain. In particular, the microscopic structure of clay suspensions on submicron-length scales has not yet been quantitatively examined.

In this study, we aimed to investigate the microscopic structure of vermiculite clay suspensions with Cs^+ as a function of the adsorbed Cs^+ concentration and elucidate the relationship between the structure of vermiculite and the adsorption of Cs^+ to vermiculite. These findings provide important fundamental information about the stability and desorption of Cs^+ on clay particles. Therefore, our study should contribute to (i) predicting the environmental fate of radioactive cesium in contaminated areas, and (ii) developing a method to extract radioactive cesium from contaminated soil. Here, we report and discuss the SAXS profiles obtained for vermiculite suspensions containing adsorbed Cs^+ [23,24,28,29] in conjunction with the adsorption behavior of Cs^+.

Results

SAXS investigation of cesium adsorbed vermiculite. Vermiculite clay, obtained from Fukushima, Japan, was sonicated to fragment it in suspension. The dried clay powder (200 mg w_{verm}), was dispersed in aqueous CsCl solutions (20 mL) of five Cs^+ concentrations ($[Cs^+]_{ini}$) from 1 to 1000 ppm (see Table 1) for one month. The vermiculite clay initially incorporated hydrated Mg^{2+} in the interlayer spaces. The Mg^{2+} originally occupying the interlayer spaces should exchange with Cs^+ as $[Cs^+]_{ini}$ increases. The amount of Cs^+ adsorbed to the vermiculite clay, evaluated by inductively coupled plasma mass spectrometry (ICP-MS), increased with $[Cs^+]_{ini}$. Each suspension was directly measured by SAXS. The observed X-ray scattering intensities as a function of the magnitude of the scattering vector q [$= (4\pi/\lambda)\sin(\theta)$; λ is the incident X-ray wavelength and 2θ is the scattering angle], $I_{obs}(q)$, were normalized by time and the second moment of the intensity, Q, which is proportional to the mean square scattering length density fluctuation[30,31],

$$Q = \int_0^\infty q^2 I_{obs}(q)dq \propto 2\pi^2 \phi_{clay}\left(1-\phi_{clay}\right)\Delta\rho^2 \quad (1)$$

Here, ϕ_{clay} is the volume fraction of the clay particles. $\Delta\rho$ is the scattering contrast between the clay and the solvent and $\Delta\rho = (\rho_{clay} - \rho_{water})$ where ρ_{clay} and ρ_{water} are the scattering length density of clay and of water. In each sample, ϕ_{clay} was not known because of sedimentation; therefore, $I_{nor}(q)$ ($= I_{obs}(q)/Q$) was used to remove the effect of the volume fraction. Thus, we could compare the change in intensity as a function of w_{Cs}, which is the weight of Cs^+ adsorbed to 200 mg of vermiculite clay (see Table 1).

Figure 1 shows $I_{nor}(q)$ as a function of q for samples 1–5 (see Table 1) on a double logarithmic scale. The profiles reflect the structural changes in the vermiculite clay induced by the exchange of Mg^{2+} with Cs^+ in suspension. In the low-q region of $q < 0.1$ Å^{-1}, the scattering intensity starts to increase in accordance with the power law for scattering, $I(q) \approx q^{-\beta}$ with $\beta \approx 3$. In the high-q region of $q > 0.3$ Å^{-1}, the scattering maxima at around $q_m = 0.42$ Å^{-1}, indicated by P_1 in Fig. 1, are observed. The peaks arise from the interference between the stacked clay sheets[18,28]. The distance between neighboring clay sheets ($D = 2\pi/q_m$) can be estimated as approximately 14.9 Å in samples 1–3. The Bragg diffraction peak shows long tailing toward higher q in sample 4. This shoulder peak, (P_2 in Fig. 1), originates from the interlayer spaces intercalating with the partially dehydrated Cs^+. In the SAXS profile of sample 5, this peak shifts to a higher value of q and its intensity decreases. The peak is hardly visible around $q = 0.49$ Å^{-1}. This abrupt decrease in the intensity is attributed to the large distribution of D and the decrease of the stacking number, N, per crystal domain.

Only sample 1 shows a broad peak at $q = 0.18$ Å^{-1} (arrow and P_3 in Fig. 1). This peak is attributed to long-range inhomogeneity in the stacking state of the 2 : 1 phyllosilicate clay sheets, and the length of the inhomogeneity can be roughly calculated as 35 Å from the peak position. The origin of this broad peak is the swollen interlayer spaces in the stacked clay sheets. These spaces can be formed in the crystal domains at a lower Cs^+ adsorption ($w_{Cs} = 0.018$ mg).
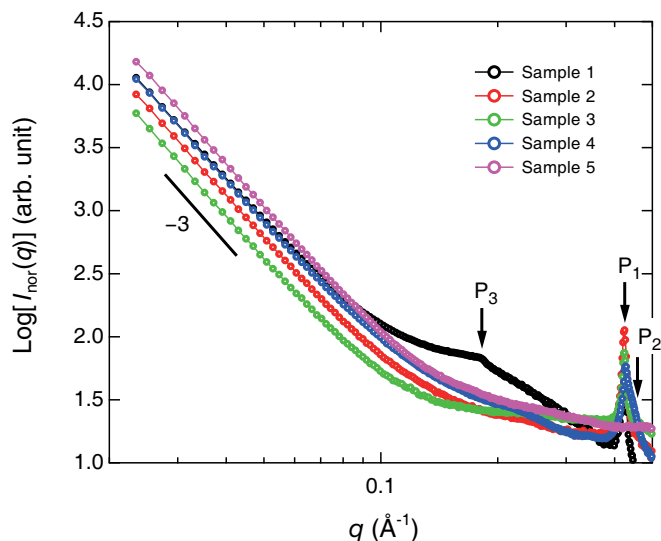

Figure 1 | Structural changes in the vermiculite/Cs^+ suspension on the nano scale. Double-logarithmic plots of the SAXS profiles obtained for Cs^+ adsorbed on vermiculite in aqueous suspension at different w_{Cs} for samples 1 (black circles), 2 (red circles), 3 (green circles), 4 (blue circles), and 5 (pink circles). The peaks indicated by P_1 and P_2 originate from the interference between the stacked clay sheets. The peak indicated by P_3 is attributed to long-range inhomogeneity in the stacking of the clay sheets.

Scattering model for clay suspension. Because vermiculite clay is a 2 : 1 phyllosilicate multilayer composed of two tetrahedral sheets and one octahedral sheet, it is reasonable to assume that the scattering intensity at the small-angle region is increased by stacked thin sheets. The small-angle scattering intensity, $I(q)$, can be described by

$$I(q) \propto P(q) \times S(q) \quad (2)$$

where $P(q)$ is the form factor, which represents the shape of a single sheet[32,33], and $S(q)$ is the structure factor for one-dimensionally overlapping plates perpendicular to the plane[32,34–36]. It is assumed that the clay sheet is a disk with a base of radius R and thickness d; therefore, $P(q)$ is given by

$$P(q_{//},q_\perp) = \left\{\pi R^2 d \frac{2J_1(q_{//}R)}{q_{//}R}\frac{\sin(q_\perp d/2)}{q_\perp d/2}\right\}^2 \quad (3)$$

where $J_1(x)$ is the cylindrical Bessel function of the first order, and $q_{//}$ and $q_\perp$ are scattering vectors pointing in the in-plane and out-of-plane directions to the base, respectively. The structure factor describes a one-dimensional array of N sheets at interval distance D,

$$S(q_\perp) = 1 + \exp(-\frac{q_\perp^2 \sigma_D^2}{2})\frac{2}{N}\sum_{n=1}^{N-1}(N-n)\cos(q_\perp Dn)$$
$$= 1 + \exp(-\frac{q_\perp^2 \sigma_D^2}{2})\frac{N-1+\cos(q_\perp DN)-N\cos(q_\perp D)}{N\{\cos(q_\perp D)-1\}} \quad (4)$$

where σ_D is the standard deviation of each position based on the Gaussian distribution[35–37]. We assume that the stacked layers form particles and the orientation of the particles is random. In this case, the observed intensity is expressed by

$$I(q) \propto \int_0^{\pi/2} P(q\sin\alpha, q\cos\alpha)S(q\cos\alpha)\sin\alpha d\alpha \quad (5)$$

Here, α is the angle between a reference axis and the principal axis of the layers[33]. To evaluate the data quantitatively, the resolution of the instrument and the distributions of R and D are included.

Table 1 | Compositions determined by ICP-MS for suspensions of vermiculite with Cs^+

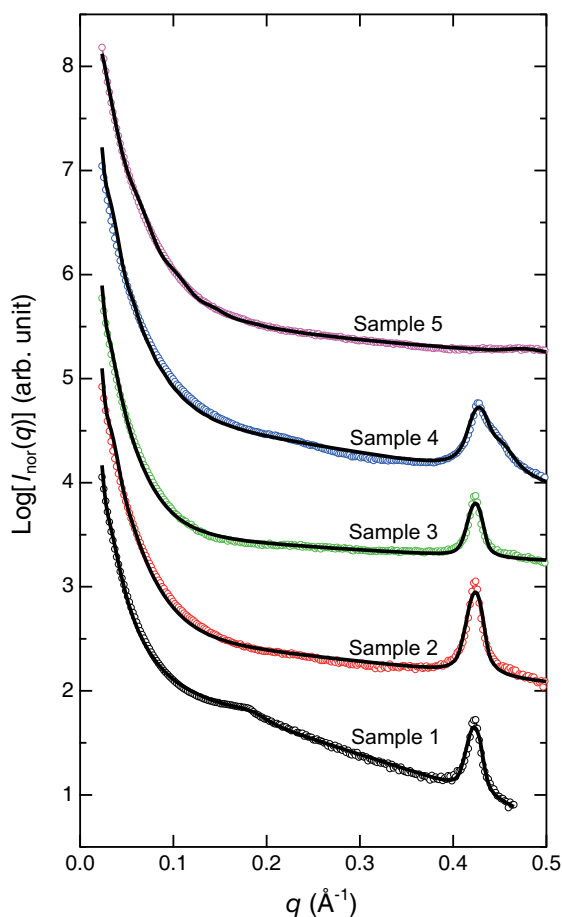| Sample No.	$[Cs^+]_{ini}$ (ppm)	w_{verm} (mg)	w_{Cs} (mg)	ϕ_{Cs} (wt %)	pH
1	1	200	0.018	90.1	6.76
2	5	200	0.099	98.7	6.89
3	20	200	0.384	96.1	6.72
4	100	200	1.97	95.1	6.45
5	1000	200	6.94	34.7	6.41

Figure 2 | Numerical analyses of SAXS intensity distribution. The SAXS profiles are vertically shifted to avoid overlap by an offset constant of 1, and the constant values for samples 1–5 are 0, 1, 2, 3, and 4, respectively. The scattering profile of sample 1 is shown on a net intensity scale of $\log[I_{nor}(q)]$. The solid black lines are best-fit theoretical profiles obtained by using equation (2) together with the characteristic parameters and error (Table 2).

Quantitative analyses of SAXS intensity distributions. The solid lines in Fig. 2 show the best-fit theoretical scattering curves. The theoretical profiles reproduce the experimentally observed SAXS profiles well over a wide q.

The power law scattering with the exponent $\beta \approx 3$ at low q ($q < 0.1$ Å^{-1}) is related to two parameters, R and N (equations (3) and (4)). When R or N increases, the scattering intensity in the low-q region tends to shift further toward the low-q region, because the size of the scatterer becomes large. N also affects the peak width; as N increases, the peak width narrows. Therefore, R and N must be evaluated simultaneously for quantitative data analysis.

For double Bragg peaks (samples 1 and 4), equation (4) can be modified as

$$S(q_\perp) = 1 + f_1 \exp\left(-\frac{q_\perp^2 \sigma_{D,1}^2}{2}\right) \frac{N - 1 + \cos(q_\perp D_1 N) - N\cos(q_\perp D_1)}{N\{\cos(q_\perp D_1) - 1\}}$$
$$+ f_2 \exp\left(-\frac{q_\perp^2 \sigma_{D,2}^2}{2}\right) \frac{N - 1 + \cos(q_\perp D_2 N) - N\cos(q_\perp D_2)}{N\{\cos(q_\perp D_2) - 1\}} \quad (6)$$

where D_1 and D_2 are the interlayer distances, and $\sigma_{D,1}$ and $\sigma_{D,2}$ are the corresponding standard deviations[37] in the single crystal domain. We assume that random distribution of the different spaced layers, and the fractions are given by f_1 and f_2 ($f_1 + f_2 = 1$), respectively. Only one Bragg peak is observed in samples 2, 3, and 5, and $f_1 = 1$ and $f_2 =$

Table 2 | Characteristic parameters determined by model analysis of SAXS for aqueous suspensions of vermiculite with Cs$^+$

Sample No.	R (Å)	σ_R (Å)	N	f_1	f_2	D_1 (Å)	D_2 (Å)	$\sigma_{T,1}$ (Å)	$\sigma_{T,2}$ (Å)	$\sigma_{D,1}$ (Å)	$\sigma_{D,2}$ (Å)
1	168 ± 4.4	33.1 ± 2.9	90.4 ± 14.3	0.73	0.27	14.9 ± 0.1	33.5 ± 0.5	0.44 ± 0.07	5.97 ± 0.72	4.37 ± 0.04	11.5 ± 0.4
2	164 ± 4.5	28.7 ± 2.6	98.8 ± 20.4	1	0	14.9 ± 0.1	–	0.50 ± 0.07	–	3.25 ± 0.04	–
3	169 ± 4.3	31.5 ± 2.3	91.8 ± 16.4	1	0	14.9 ± 0.1	–	0.44 ± 0.09	–	3.37 ± 0.04	–
4	166 ± 4.5	25.5 ± 2.7	53.7 ± 7.9	0.79	0.21	14.7 ± 0.1	14.0 ± 0.2	0.55 ± 0.08	1.50 ± 0.10	4.03 ± 0.05	0.54 ± 0.1
5	165 ± 8.1	83.1 ± 4.8	25.5 ± 3.5	1	0	12.6 ± 0.3	–	1.66 ± 0.25	–	4.48 ± 0.10	–

0 in equation (6) for these samples. The distribution of D_1 and D_2 is calculated from the Gaussian profile of the standard deviation, $\sigma_{T,1}$ and $\sigma_{T,2}$, respectively.

The parameters R, σ_R, N, f_i, D_i, $\sigma_{T,i}$, and $\sigma_{D,i}$ ($i = 1$ or 2) were refined to give the best fit to the experimental SAXS profiles (Table 2). The thickness of the clay sheet, d, was fixed as 6.6 Å in this numerical analysis. This is because the two tetrahedral clay sheets and one octahedral clay sheet that form the unit of the 2 : 1 phyllosilicate vermiculite clay sheet have an exact thickness of 2.2 Å[38]. The polydispersity of N was not required in order to fit the data. The solid lines in Fig. 2 show the best-fit theoretical scattering curves.

Discussion

Figure 3 shows the extracted parameters D_i and N plotted as a function of w_{Cs} to characterize the structural changes in the crystal domain of vermiculite clay. In Fig. 3a, two characteristic distances, $D_1 = 14.9$ Å and $D_2 = 33.1$ Å, are observed at $w_{Cs} = 0.018$ mg (sample 1), where f_1 and f_2 are 0.73 and 0.27, respectively. One component, containing a large swollen interlayer space (= 33.1 Å; Table 2) in the crystal domain, disappears as the $[Cs^+]_{ini}$ increases, and only the other component remains in the SAXS profile at $w_{Cs} = 0.099$ mg (sample 2) and D_1 remains as 14.9 Å. This indicates that only large swollen layers shrink, because the values of N for samples 1 and 2 are virtually unchanged (Fig. 3b and Table 2). Therefore, we expect that at lower $[Cs^+]_{ini}$, some Cs^+ preferentially intercalates in the wide swollen interlayer spaces in addition to adsorption at the edge or planar sites in the crystal domains, whereas the narrower interlayer spaces are not affected.

At $w_{Cs} = 1.97$ mg (sample 4), we estimate that the distance between neighboring sheets decreases in about 20% of the layers (Table 2; $D_2 = 14.0$ Å, $f_2 = 0.21$), whereas D_1 is 14.7 Å for $f_1 = 0.79$. Two peaks are clearly visible, which is evidence of the collective intercalation of Cs^+. Accordingly, the exchange between the partially dehydrated Cs^+ and hydrated Mg^{2+} should proceed in the selective interlayers above $w_{Cs} = 0.384$ mg (sample 3). At $w_{Cs} = 6.94$ mg (sample 5), D_1 is 12.6 Å. It has been reported that the value of D_1 decreases to approximately 10.5 Å for the dry powder[28], which may be partially swollen in suspensions.

The small-angle scattering intensities and the power law below $q = 0.1$ Å^{-1} increases with $[Cs^+]_{ini}$ from sample 3 to 5 (Fig. 1). Our quantitative analyses suggest that this is caused by the decrease in the stacking number, N, at $w_{Cs} > 0.384$ mg (Fig. 3b), whereas R is similar in all samples.

Therefore, the changes in both the interlayer space and the stacking number probably originate from the cationic exchange of hydrated Mg^{2+} with partially hydrated Cs^+. The shrinkage may induce local strain and defects in the crystal domains, which leads to the segmentation of the stacking clay sheets. Next, we describe the effect of the electrostatic interactions in the layer space in relation to Cs^+ adsorption. The direct coordination of a partially dehydrated Cs^+ to oxygen atoms in the SiO_4 tetrahedral sheet, which has a negative charge, locally shields the layer charge of the SiO_4 tetrahedral sheet[23,24,29]. This reduces the local electron charge density on the opposite surface of the SiO_4 tetrahedral sheet. The attractive interaction between the SiO_4 tetrahedral sheet and hydrated Mg^{2+} is weakened, further swelling occurs in the layer space, and partial abruption takes place in the hydrated Mg^{2+} layer spaces. Consequently, the crystal domain undergoes segmentation and N (the grain size of the crystal domain) should decrease (Fig. 3b) when a sufficient amount of Cs^+ intercalates in the local layer space. The segmented smaller-crystal domain generates new planar regions, which are covered by hydrated Mg^{2+}. This planar region is expected to serve as a specific adsorption site for Cs^+, in addition to the interlayer spaces. Two Cs ions can coordinate directly to an oxygen atom in the SiO_4 tetrahedral sheets through the exchange with one hydrated Mg^{2+}, implying that Cs^+ intercalation in the swelling layer space of vermiculite clay promotes further Cs^+ adsorption at the freshly generated crystal domain interface.

The dashed line in Fig. 3b is a single exponential function, $\exp(-w_{Cs}/w_{Cs}^*)$, which roughly reproduces the change in N with w_{Cs}, where $w_{Cs}^* = 0.39$. Thus, the segmentation gradually starts well below $w_{Cs}^*/10 \approx 0.04$ mg (thick arrow, Fig. 3b). Once one partially dehydrated Cs^+ exchanges with a hydrated Mg^{2+} in a vermiculite interlayer space, the other Cs^+ is likely to occupy the neighboring adsorption site in the same layer space. If Mg^{2+} occupies the neighboring site to an intercalating Cs^+, a difference in the layer spaces arises at the neighboring adsorption sites increasing the local strain energy of the clay sheet compared with Cs^+ occupancy. Furthermore, Okumura and coworkers examined the adsorption mechanism of Cs^+ in clay minerals by high-resolution transmission electron microscopy imaging in mica. They reported that some Cs ions are collectively located in the layer spaces and did not exchange individually
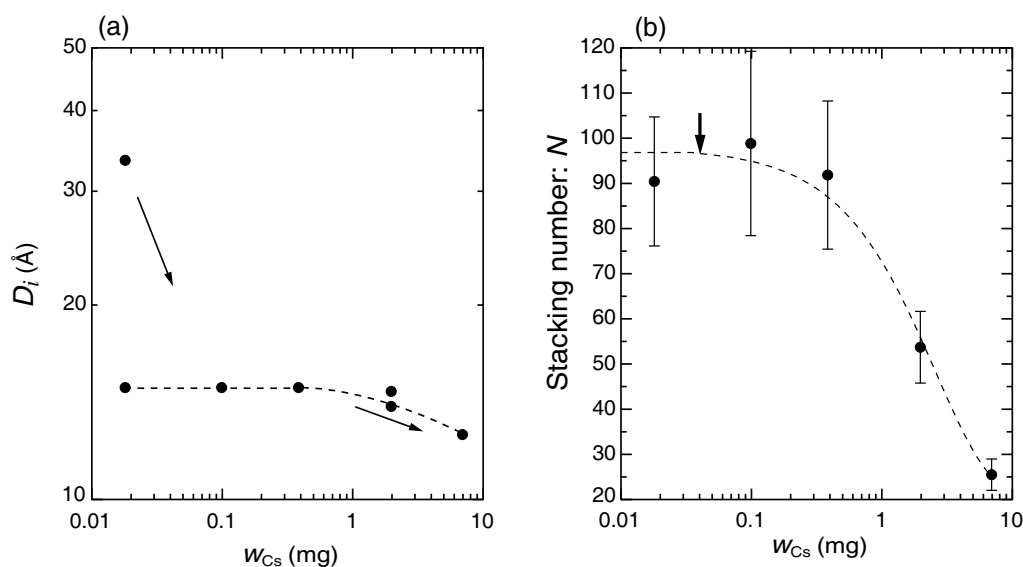

Figure 3 | Structural changes in the crystal domain of vermiculite. (a) D_i and (b) N with the error plotted as a function of w_{Cs} on logarithmic and linear scales, respectively. Dashed lines in (a) and (b) are a visual guide and single exponential function, $\exp(-w_{Cs}/w_{Cs}^*)$, respectively. The arrow in (a) is a visual guide. Errors in D_i in the numerical SAXS analyses are within ±3% accuracy. Error bars of D_i are omitted for clarity.
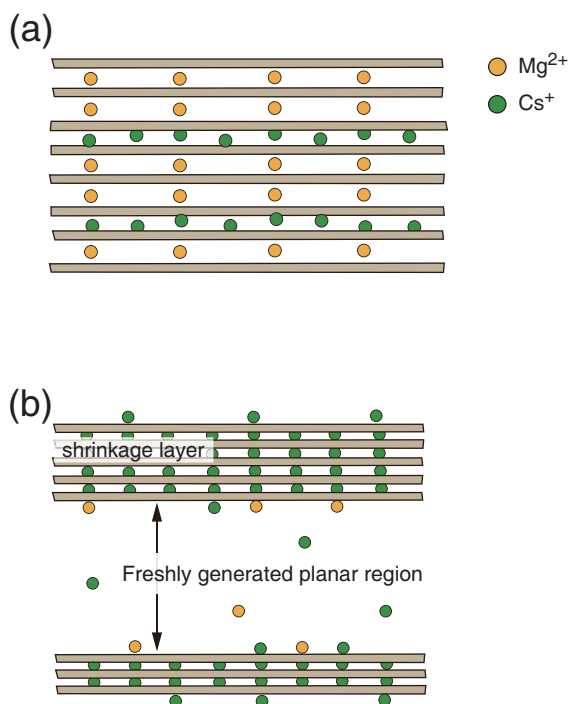
Figure 4 | Collective structural changes induced by Cs⁺ adsorption to vermiculite clay. Schematic illustrations of the crystal domain of vermiculite clay with Cs⁺. (a) Collective intercalation (localization) of Cs⁺ in the selective layer spaces and (b) segmentation of the crystal domain of vermiculite clay, providing fresh planar adsorption sites for Cs⁺.

with a hydrated Mg^{2+}[39]. Based on these observations and our results, the adsorption behavior of Cs⁺ in vermiculite clay in suspension can be well characterized by two competitive phenomena: (i) localization of partially dehydrated Cs⁺ in the selective interlayer spaces caused by collective adsorption (Fig. 4a) and (ii) segmentation of the crystal domain (Fig. 4b) shown in the SAXS profiles, that provides fresh planar adsorption sites for Cs⁺. The contributions of (i) and (ii) should account for the intriguing structural changes in the vermiculite/Cs⁺ suspension.

Vermiculite clays are ubiquitous in the soil around Fukushima[40], and they exhibit high affinity for adsorbing radioactive cesium compared with other minerals. Our work should help to predict the environmental fate of radioactive cesium in the polluted soils at Fukushima, which is very important for radiation protection and decontamination.

Methods

Materials. Vermiculite clay from Ishikawa-Gun, Fukushima, Japan, extracted from the soil, was purchased from Geo-Science Materials Nichika Co., Ltd. (Kyoto, Japan). Details of this material are available elsewhere[41]. Reagent grade CsCl was purchased from Wako Pure Chemical Industries, Co., Ltd. (Osaka, Japan) and used without further purification. The water used in this study was deionized with a Milli-Q purification system (Merck Millipore, Billerica, MA).

X-Ray fluorescence measurements. The chemical composition of vermiculite clay was determined with an X-ray fluorescence (XRF) spectrometer (ZSX Primus II XRF, Rigaku Co. Ltd., Tokyo, Japan). Measurements took 20 min and were conducted at room temperature in vacuo. Dry, powdered vermiculite clay powder was placed on a 10 mm sample plate (Cat. No. RS540-10, Rigaku), and a small amount of powder was packed into a special cell (Cat. No. 33990051, Rigaku) for quantitative analysis of the atomic composition. The chemical composition of vermiculite used in this study was evaluated as $(Mg_{0.41}Ca_{0.01}K_{0.01})(Mg_{2.55}Ni_{0.01}Fe_{0.42}\ Cr_{0.01}Al_{0.01})(Si_{2.71}Al_{1.29})O_{10}(OH)_2$.

X-ray diffraction measurements. A diffractometer (M03XHF22, MAC Science Co., Ltd., Tokyo, Japan) was used to obtain the X-ray diffraction (XRD) data for vermiculite powder to confirm its purity. The measurements were performed at room temperature with a Cu-Kα line generating an incident wavelength of 1.54 Å and with

an angle (θ) step of 0.04° for $2\theta = 2$ to 120°. Vermiculite clay was crushed briefly in a mortar before the XRD measurements. The XRD profile is shown in the supplementary information. The peak position originates from the interference between the 2 : 1 phyllosilicate clay sheet structures and corresponds well to the previous results for vermiculite containing hydrated Mg^{2+} (verm-Mg) in the interlayer spaces[18,26]. The peak is indicated by thick arrows in supplementary data 1. The average distance between the neighboring stacked clay sheets is calculated as 14.4 Å from the peak position. Because no impurities are observed in the XRD profile, the vermiculite clay is very pure. The atomic composition of vermiculite and its XRD profile suggest that, initially, hydrated Mg^{2+} occupies the interlayer space.

Sample preparation for SAXS. Vermiculite clay (2 g) in water (50 mL) was sonicated with an ultrasonicator (XL2020, Misonix Co., Ltd., Farmingdale, NY) in pulse mode at 80% intensity for 60 min to disperse the verm-Mg clay. Vermiculite clay was collected by filtration and then dried at 40°C. The dried powder (200 mg) was dispersed in aqueous CsCl solution (20 mL) at five Cs⁺ concentrations, ranging from 1 to 1000 ppm (Table 1) for one month. The range of pH values for sample 1 to 5 at 25°C was between 6.41 and 6.89 after one month (see Table 1). Each suspension was directly measured by SAXS.

After reaching adsorption equilibrium between Cs⁺ and vermiculite clay, the amount of Cs⁺ adsorbed to the vermiculite clay was evaluated by ICP-MS (NexION 300D, PerkinElmer Co., Ltd., Kanagawa, Japan), as follows. First, the suspension was centrifuged at 8000 rpm for 15 min and the vermiculite containing adsorbed Cs⁺ precipitated. The supernatant liquid was sampled and diluted with 0.1 N HNO₃, filtered through a cellulose nitrate membrane (0.45 μm; Merck Millipore), and analyzed by ICP-MS to determine the Cs⁺ concentration ($[Cs^+]_{sup}$). The values of w_{Cs} and the weight rate (%) of Cs⁺ adsorption to vermiculite with respect to $[Cs^+]_{ini}$ (ϕ_{Cs}; see Table 1) were calculated from $[Cs^+]_{sup}$. In addition to Cs⁺ detection by ICP-MS, Mg^{2+} in the supernatant liquid was confirmed in all of the samples. The concentration of Mg^{2+} in the supernatant liquid gradually increased from sample 1 to 5. This implies that Cs⁺ adsorption to vermiculite clay occurs through the ion-exchange mechanism.

SAXS experiments. SAXS measurements were performed using X-ray diffraction apparatus (NANO-Viewer, Rigaku). The incident X-ray beam was generated from a Cu-Kα line (wavelength $\lambda = 1.54$ Å) and was focused to a spot 450 μm in diameter at the sample position with a confocal optic (Max-Flux, Rigaku) equipped with a pinhole slit collimator. The scattered X-rays from the sample were detected by a two-dimensional position-sensitive detector (Pilatus 100K/R, Rigaku), with 195×487 pixels (33.5×83.8 mm) and a spatial resolution of 0.172 mm, covering a q range of $(0.02\ \text{Å} < q < 0.5\ \text{Å}^{-1})$ at a sample-to-detector distance of 325 mm. The scattering data recorded on the detector were corrected for counting efficiency, instrumental background, and air scattering on a pixel-to-pixel basis. The X-ray scattering intensity distribution, $I(q)$, was circularly averaged. The sample solutions were loaded into glass capillary cells with 0.01-mm-thick walls and a 2.0 mm sample thickness. All X-ray scattering data were acquired at 25°C. Cell scattering and solvent (H₂O) scattering were subtracted from $I(q)$ by considering the transmission and the volume fraction of H₂O in the sample solution.

SAXS data analyses. To examine the effect of the Cs⁺, the SAXS profiles were evaluated by the following method. Because the vermiculite samples were unlikely to disperse homogeneously in the glass capillary cell during the SAXS measurements owing to the specific gravity, the scattering intensity was not plotted on a relative scale. To overcome this limitation, $I_{obs}(q)$ was normalized to Q[30,31], which allowed the scattering profiles to be compared on a relative intensity scale (see equation (1)). To calculate Q, the upper cutoff for the integration was defined as $q_{max} = 0.5$ Å⁻¹ instead of infinity, where $q_{max} = 0.5$ Å⁻¹ is sufficiently large for the continuum approximation.

The finite resolution of the instruments can be incorporated by convoluting the ideal scattering intensity and the resolution function, which was approximated by a Gaussian profile of the standard deviation, $\Delta q = 0.0051$ Å. The value of Δq used in this study was calculated in accordance with the literature[42]. $P(q)$ in equation (3) varies slowly with q in the q-region, whereas $S(q)$ produces a sharp peak and varies rapidly. Therefore, the effect of finite instrumental resolution is used for only the structure factor.

The distribution of R had to be considered to reproduce the scattering intensities precisely, so that the Schultz distribution with the corresponding standard deviation, σ_R, was used, which could contribute to enhance computation rate[43]. In equation (4), the distribution of D was also included based on the Gauss distribution with the standard deviation $\sigma_{T,i}$, which reflected the calculations with equation (6).

1. Morino, Y., Ohara, T. & Nishizawa, M. Atmospheric Behavior, Deposition, and Budget of Radioactive Materials from the Fukushima Daiichi Nuclear Power Plant in March 2011. *Geophys. Res. Lett.* **38**, L00G11 (2011).
2. Hosoda, M. *et al.* The Time Variation of Dose Rate Artificially Increased by the Fukushima Nuclear Crisis. *Sci. Rep.* **1**, 87 (2011).
3. Brumfiel, G. & Fuyuno, I. Fukushima's Legacy of Fear. *Nature* **483**, 138–140 (2012).
4. Brumfiel, G. Fukushima's Doses Tallied. *Nature* **485**, 485, 423–424 (2012).
5. Koarashi, J. *et al.* Retention of Potentially Mobile Radiocesium in Forest Surface Soils Affected by the Fukushima Nuclear Accident. *Sci. Rep.* **2**, 1005 (2012).
6. du Bois, P. B. *et al.* Estimation of Marine Source-term Following Fukushima Dai-ichi Accident. *J. Environ. Radioact.* **114**, 2–9 (2012).

7. Hirose, K. 2011 Fukushima Dai-ichi Nuclear Power Plant Accident: Summary of Regional Radioactive Deposition Monitoring Results. *J. Environ. Radioact.* **111**, 13–17 (2012).

8. Endo, S. *et al.* Measurement of Soil Contamination by Radionuclides due to the Fukushima Dai-ichi Nuclear Power Plant Accident and Associated Estimated Cumulative External Dose Estimation. *J. Environ. Radioact.* **111**, 18–27 (2012).

9. Brumfiel, G. Fallout of Fear. *Nature* **493**, 290–293 (2013).

10. Morino, Y. *et al.* Episode Analysis of Deposition of Radiocesium from the Fukushima Daiichi Nuclear Power Plant Accident. *Env. Sci. Tech.* **47**, 2314–2322 (2013).

11. Okumura, M., Nakamura, H. & Machida, M. Mechanism of Strong Affinity of Clay Minerals to Radioactive Cesium: First-Principles Calculation Study for Adsorption of Cesium at Frayed Edge Sites in Muscovite. *J. Phys. Soc. Jpn.* **82**, 033802-0033802-5 (2013).

12. Sawhney, B. L. Selective Sorption and Fixation of Cations by Clay Minerals: A Review. *Eur. Clays Clay Miner.* **20**, 93–100 (1972).

13. Comans, R. N. J. & Hockley, D. E. Kinetics of Cesium Sorption on Illite. *Geochim. Cosmochim. Acta* **56**, 1157–1164 (1992).

14. Cornell, R. M. Adsorption of Cesium on Minerals -A Review. *J. Radioanal. Nucl. Chem.* **171**, 483–500 (1993).

15. Hird, A. B., Rimmer, D. L. & Livens, F. R. Total Cesium-Fixing Potentials of Acid Organic Soils. *J. Environ. Radioact.* **26**, 103–118 (1995).

16. Maes, E., Vielvoye, L., Stone, W. & Delvaux, B. Fixation of Radiocaesium Traces in a Weathering Sequence Mica -> Vermiculite -> Hydroxy Interlayered Vermiculite. *Eur. J. Soil Sci.* **50**, 107–115 (1999).

17. Nakao, A., Funakawa, S., Watanabe, T. & Kosaki, T. Pedogenic Alterations of Illitic Minerals Represented by Radiocaesium Interception Potential in Soils with Different Soil Moisture Regimes in Humid Asia. *Eur. J. Soil Sci.* **60**, 139–152 (2009).

18. Kogure, T. *et al.* XRD and HRTEM Evidence for Fixation of Cesium Ions in Vermiculite Clay. *Chem. Lett.* **41**, 380–382 (2012).

19. Comans, R. N. J., Haller, M. & Depreter, P. Sorption of Cesium on Illite - Nonequilibrium Behavior and Reversibility. *Geochim. Cosmochim. Acta* **55**, 433–440 (1991).

20. Sawhney, B. L. Sorption and Fixation of Microquantities of Cs by Clay Minerals: Effect of Saturating Cations. *Soil Sci. Soc. Am. Proc.* **28**, 183–186 (1964).

21. Kim, Y., Cygan, R. T. & Kirkpatrick, R. J. Cs-133 NMR and XPS Investigation of Cesium Adsorbed on Clay Minerals and Related Phases. *Geochim. Cosmochim. Acta* **60**, 1041–1052 (1996).

22. Poinssot, C., Baeyens, B. & Bradbury, M. H. Experimental and Modelling Studies of Ceasium Sorption on Illite. *Geochim. Cosmochim. Acta* **63**, 3217–3227 (1999).

23. Bostick, B. C., Vairavamurthy, M. A., Karthikeyan, K. G. & Chorover, J. Cesium Adsorption on Clay Minerals: An EXAFS Spectroscopic Investigation. *Environ. Sci. Technol.* **36**, 2670–2676 (2002).

24. Fan, Q. H. *et al.* An EXAFS Study on the Effects of Natural Organic Matter and the Expandability of Clay Minerals on Cesium Adsorption and Mobility. *Geochim. Cosmochim. Acta* **135**, 49–65 (2014).

25. Nakao, A., Thiry, Y., Funakawa, S. & Kosaki, T. Characterization of the Frayed Edge Site of Micaceous Minerals in Soil Clays Influenced by Different Pedogenetic Conditions in Japan and Northern Thailand. *Soil Sci. Plant Nutr.* **54**, 479–489 (2008).

26. Bear, F. E. *Chemistry of the Soil*. Van Nost Reinhold: New York, 1964.

27. Maes, A. & Cremers, A. Charge Density Effects in Ion Exchange. Part 2.— Homovalent Exchange Equilibria. *J. Chem. Soc. Faraday. Trans.* **74**, 1234–1241 (1978).

28. Morimoto, K. *et al.* Desorption of Cs$^+$ Ions Intercalated in Vermiculite Clay through Cation Exchange with Mg^{2+} Ions. *Chem. Lett.* **41**, 1715–1717 (2012).

29. Qin, H. B. *et al.* Investigation of Cesium Adsorption on Soil and Sediment Samples from Fukushima Prefecture by Sequential Extraction and EXAFS Technique. *Geochem. J.* **46**, 297–302 (2012).

30. Glatter, O. & Kratky, O. *Small Angle X-ray Scattering* (Academic Press, 1982).

31. Higgins, J. S. & Benoît, H. C. *Polymers and Neutron Scattering* (Oxford University Press, 1994).

32. Roe, R. J. *Methods of X-ray and Neutron Scattering in Polymer Science* (Oxford University Press, 2000).

33. Endo, H., Miyazaki, S., Haraguchi, K. & Shibayama, M. Structure of Nanocomposite Hydrogel Investigated by means of Contrast Variation Small-Angle Neutron Scattering. *Macromolecules* **41**, 5406–5411 (2008).

34. Guinier, A. *X-ray Diffraction in Crystal, Imperfect Crystal, and Amorphous Bodies* (WH Freeman, 1963).

35. Nallet, F., Laversanne, R. & Roux, D. Modeling X-Ray or Neutron-Scattering Spectra of Lyotropic Lamellar Phases - Interplay between Form and Structure Factors. *J. Phys. II France* **3**, 487–502 (1993).

36. Richter, D. *et al.* Polymer Aggregates with Crystalline Cores: The System Polyethylene-Poly(ethylenepropylene). *Macromolecules* **30**, 1053–1068 (1997).

37. Squires, G. L. *Introduction to the Theory of Thermal Neutron Scattering,* Cambridge University Press: Cambridge, 1978.

38. Brindley, G. W. & Brown, G. *Interstratified Clay Minerals. Crystal Structures of Clay Minerals and their X-ray Identification* (Mineralogical Society, 1980).

39. Okumura, T. *et al.* Direct Observation of Cesium at the Interlayer Region in Phlogopite Mica. *Microscopy* **63**, 65–72 (2014).

40. Shimane, H. *Vermiculite and Allied Minerals.* In: *The clays of Japan.* [Editorial Subcommittee for the Clays of Japan Organizing Committee, International Clay Conference (ed.)][139–142]. (Geological Survey of Japan, 1969).

41. Sudo, T. & Shimoda, S. *Clays and Clay Minerals of Japan* (Elsevier, 1978).

42. Pedersen, J. S., Posselt, D. & Mortensen, K. Analytical Treatment of the Resolution Function for Small-Angle Scattering. *Journal of Applied Crystallography* **23**, 321–333 (1990).

43. Bartlett, P. & Ottewill, R. H. A Neutron Scattering Study of the Structure of a Bimodal Colloidal Crystal. *J. Chem. Phys.* **96**, 3306–3318 (1992).

Acknowledgments

Author contributions

R.M. and H.E. designed and led the research, carried out experiments and data analysis, and documented the findings; R.M., H.E. and S.Y. wrote the manuscript and prepared the figures. S.N. designed the small-angle X-ray scattering experiments. T.K., S.S. and T.Y. participated in scientific discussions. All authors contributed to the interpretation of results and to the finalization of the submitted manuscript.

Additional information